

# Metavalent Bonding–Induced Phonon Hardening and Giant Anharmonicity in BeO

Xuejie Li,<sup>1</sup> Yuzhou Hao,<sup>1</sup> Yujie Liu,<sup>1</sup> Shengying Yue,<sup>2</sup> Xiaolong Yang,<sup>3,4,†</sup>

Turab Lookman,<sup>5</sup> Xiangdong Ding,<sup>1</sup> Jun Sun,<sup>1</sup> and Zhibin Gao<sup>1,\*</sup>

<sup>1</sup>*State Key Laboratory for Mechanical Behavior of Materials,  
State Key Laboratory of Porous Metal Materials, School of Materials Science and Engineering,  
Xi'an Jiaotong University, Xi'an, 710049, China*

<sup>2</sup>*Laboratory for Multiscale Mechanics and Medical Science,  
State Key Laboratory for Strength and Vibration of Mechanical Structures,  
School of Aerospace, Xi'an Jiaotong University, Xi'an 710049, China*

<sup>3</sup>*College of Physics, Chongqing Key Laboratory for Strongly Coupled Physics,  
Chongqing University, Chongqing 401331, China*

<sup>4</sup>*Center of Quantum Materials and Devices, Chongqing University, Chongqing 401331, China*

<sup>5</sup>*AiMaterials Research LLC, Santa Fe, NM 87501, United States*

(Dated: November 17, 2025)

The search for materials with intrinsically low thermal conductivity ( $\kappa_L$ ) is critical for energy applications, yet conventional descriptors often fail to capture the complex interplay between bonding and lattice dynamics. Here, first-principles calculations are used to contrast the thermal transport in covalent zincblende (zb) and metavalent rocksalt (rs) BeO. We find that the metavalent bonding in rs-BeO enhances lattice anharmonicity, activating multi-phonon scattering channels and suppressing phonon transport. This results in an ultralow  $\kappa_L$  of 24 W m<sup>-1</sup> K<sup>-1</sup> at 300 K, starkly contrasting with the zb phase (357 W m<sup>-1</sup> K<sup>-1</sup>). Accurately modeling such strongly anharmonic systems requires explicit inclusion of temperature-dependent phonon renormalization and four-phonon scattering. These contributions, negligible in zb-BeO, are essential for high-precision calculations of the severely suppressed  $\kappa_L$  in rs-BeO. Finally, we identify three key indicators to guide the discovery of metavalently bonded, incipient-metallic materials: (i) an NaCl-type crystal structure, (ii) large Grüneisen parameters ( $>2$ ), and (iii) a breakdown of the Lyddane-Sachs-Teller relation. These findings provide microscopic insight into thermal transport suppression by metavalent bonding and offer a predictive framework for identifying promising thermoelectrics and phase-change materials.

## I. INTRODUCTION

As the only alkaline-earth oxide that crystallizes in the wurtzite lattice rather than the cubic sodium chloride structure, beryllium oxide (BeO) exhibits remarkable properties, including low average atomic mass, high Debye temperature, exceptional hardness [1–5], outstanding thermal conductivity [6], high melting point, elevated electrical resistivity [6–9], excellent thermal stability, and superior radiation resistance [10]. These characteristics endow BeO with broad potential applications in optics, semiconductor manufacturing, power electronics [11], reactor moderating materials, and chip carrier substrates [10]. To date, extensive studies have focused on wurtzite-BeO (w-BeO), with its mechanical [12, 13], thermal [7, 14–16], and electrical properties [17]. In contrast, the other two polymorphs, i.e., zinc blende BeO (zb-BeO) and rocksalt BeO (rs-BeO), have received significantly less attention.

A recent study [18] demonstrated that the exceptionally high static dielectric constant ( $\sim 271\epsilon_0$ , where  $\epsilon_0$  is the vacuum permittivity) in rs-BeO, combined with strong electron-cloud Coulomb repulsion, induces Be-O bond elongation and consequent transverse optical (TO)

phonon softening. This phonon softening signifies a structural instability, suggesting that controlled modulation of the TO mode could offer a promising pathway for designing novel ferroelectric devices.

Building upon this insight, we emphasize that rs-BeO exhibits several distinctive features, including a softened TO phonon mode, an enhanced Born effective charge, an unusually high dielectric constant, a large Grüneisen parameter, and a moderate electrical conductivity. These properties align closely with those observed in “metavalent” solids or “incipient metals”, a class of materials known for their exceptional phase-change and thermoelectric performance, as extensively studied by Wuttig et al. [19–27].

Interestingly, our calculations confirm the Lyddane-Sachs-Teller (LST) relation holds for zb-BeO, but we observe a clear violation in rs-BeO. This deviation strongly suggests significant anharmonic effects, likely stemming from either the intrinsic structural instability of rs-BeO or the unique characteristics of metavalent bonding known to suppress longitudinal-transverse optical (LO-TO) splitting. Such pronounced anharmonicity would naturally suppress the material’s thermal conductivity.

However, this raises several fundamental questions: (i) How do these non-trivial bonding characteristics impact thermal transport? (ii) What microscopic mechanism enables metavalent bonding to enhance phonon anharmonicity and suppress thermal conductivity? (iii) rs-BeO has a large band gap and, consequently, extremely

<sup>†</sup> E-mail: yangxl@cqu.edu.cn

<sup>\*</sup> E-mail: zhibin.gao@xjtu.edu.cn

low electrical conductivity. If it is nonetheless classified as metavalently bonded, must the current definition of “incipient metals” be broadened? Answering these questions is essential for establishing clear structure–property relationships and advancing the rational design of metavalently bonded materials for thermoelectric applications.

In this work, we systematically investigate the distinct bonding characteristics of zb-BeO and rs-BeO and their correlations with electrical and thermal transport properties using first-principles calculations. Through comprehensive analysis of electronic structure, differential charge density, electron localization function, conductivity, and normalized trace of interatomic force constants, we establish that rs-BeO hallmark features of  $p$ -orbital-dominated metavalent bonding, in contrast to the conventional  $p$ -bonded covalent bonding in zb-BeO. To accurately examine lattice thermal conductivity ( $\kappa_L$ ), we explicitly account for quartic anharmonicity renormalization and off-diagonal components of heat flux operators.

We reveal that the long-range interactions inherent in the unique bonding of rs-BeO give rise to strong lattice anharmonicity, which markedly suppresses  $\kappa_L$  through multiple microscopic mechanisms, including enhanced multi-phonon scattering channels and modified phase space. These findings suggest that NaCl-type materials exhibiting large Grüneisen parameters and violation of the Lyddane-Sachs-Teller relation can serve as effective indicators for identifying promising candidates for phase-change and thermoelectric applications. The bonding-property relationships elucidated in this work provide valuable insights for the targeted design of advanced functional materials.

## II. COMPUTATIONAL METHODS

The lattice thermal conductivity ( $\kappa_L$ ) comprises particle-like ( $\kappa_p$ ) and wave-like ( $\kappa_c$ ) phonon contributions [28, 29], i.e.,  $\kappa_L = \kappa_p + \kappa_c$ . The particle-like component  $\kappa_p$  arising from the diagonal terms of the Wigner heat-flux operator is expressed as,

$$\kappa_p = \frac{\hbar^2}{k_B T^2 V N_0} \sum_{\lambda} n_{\lambda} (n_{\lambda} + 1) \omega_{\lambda}^2 \mathbf{v}_{\lambda} \otimes \mathbf{v}_{\lambda} \tau_{\lambda}, \quad (1)$$

where  $\hbar$ ,  $k_B$ ,  $V$ , and  $\omega_{\lambda}$  denote the reduced Planck constant, Boltzmann constant, primitive cell volume, and frequency of phonon mode  $\lambda$  with branch index  $s$  and wave vector  $\mathbf{q}$ , respectively. and  $N_0$  is the total number of  $\mathbf{q}$ -points sampled in the first Brillouin zone.  $\mathbf{v}_{\lambda}$  is the phonon group velocity,  $\tau_{\lambda}$  is the phonon lifetime, and  $n_{\lambda}$  represents the equilibrium phonon population obeying the Bose-Einstein distribution. Here, the phonon lifetime is solved with an iterative scheme starting with the relaxation time approximation (RTA) by incorporating the scattering contributions from isotopes, three-phonon (3ph), and four-phonon (4ph) processes.

The coherence contribution to thermal conductivity ( $\kappa_c$ ) arising from off-diagonal terms that account for wave-like tunneling effects between different vibrational eigenstates, can be mathematically formulated as,

$$\begin{aligned} \kappa_c = & \frac{\hbar^2}{k_B T^2 V N_0} \sum_{\mathbf{q}} \sum_{s \neq s'} \frac{\omega_{\mathbf{q}}^s + \omega_{\mathbf{q}}^{s'}}{2} \mathbf{v}_{\mathbf{q}}^{s,s'} \cdot \mathbf{v}_{\mathbf{q}}^{s',s} \\ & \times \frac{\omega_{\mathbf{q}}^s n_{\mathbf{q}}^s (n_{\mathbf{q}}^s + 1) + \omega_{\mathbf{q}}^{s'} n_{\mathbf{q}}^{s'} (n_{\mathbf{q}}^{s'} + 1)}{4(\omega_{\mathbf{q}}^{s'} - \omega_{\mathbf{q}}^s)^2 + (\Gamma_{\mathbf{q}}^s + \Gamma_{\mathbf{q}}^{s'})^2} \\ & \times (\Gamma_{\mathbf{q}}^s + \Gamma_{\mathbf{q}}^{s'}), \end{aligned} \quad (2)$$

where  $\Gamma_{\mathbf{q}}^s$  is the total scattering rate of a phonon mode limited by the isotope-phonon, 3ph, and 4ph processes. The  $\kappa_c$  sums the interband tunneling between any two modes ( $s$  and  $s'$ ) at the same  $\mathbf{q}$ , and becomes important when the frequency difference between the coupled phonons is smaller than their linewidths.

To capture anharmonic phonon renormalization (APRN) effects on phonon energies and thermal transport, the self-consistent phonon (SCPH) approximation has emerged as a robust approach among contemporary anharmonic lattice dynamics methods, which includes self-consistent *ab initio* lattice dynamics (SCAILD) [30] and stochastic self-consistent harmonic approximation (SSCHA) [31]. This methodology provides rigorous first-order corrections to phonon frequencies through explicit treatment of quartic anharmonicity, thereby excelling in the description of soft phonon modes and strongly anharmonic systems. Based on the theoretical foundation [32, 33], the SCPH formalism can be given by,

$$\Omega_{\lambda}^2 = \omega_{\lambda}^2 + 2\Omega_{\lambda} \sum_{\lambda_1} I_{\lambda\lambda_1}. \quad (3)$$

where in the framework of anharmonic lattice dynamics, the original harmonic phonon frequency  $\omega_{\lambda}$  undergoes temperature-dependent renormalization, yielding  $\Omega_{\lambda}$ . This transformation is governed by a scaling factor  $I_{\lambda\lambda_1}$ , which is obtained through,

$$I_{\lambda\lambda_1} = \frac{\hbar}{8N_0} \frac{V^{(4)}(\lambda, -\lambda, \lambda_1, -\lambda_1)}{\Omega_{\lambda}\Omega_{\lambda_1}} [1 + 2n_{\lambda}(\Omega_{\lambda_1})]. \quad (4)$$

Self-consistent solutions of the SCPH in Eqs. (3) and (4) require determination of two key parameters: the mode-coupling coefficient  $I_{\lambda\lambda_1}$  describing anharmonic interactions between phonon modes  $\lambda$  and  $\lambda_1$ , and the renormalized frequency  $\Omega_{\lambda}$ . The anharmonic potential in this formalism is governed by the fourth-order force constants  $V^{(4)}$ . A critical aspect of this treatment is the temperature dependence of  $I_{\lambda\lambda_1}$ , which incorporates essential quantum anharmonic effects [32, 33].

First-principles calculations were performed within the density functional theory (DFT) framework as implemented in the Vienna *ab initio* simulation package (VASP) [34, 35], employing the projector-augmented

wave (PAW) method [36, 37]. The local density approximation (LDA) was used for structural optimization, yielding equilibrium lattice constants of 3.762 Å for the zincblende (F43m, No. 216) phase and 3.586 Å for the rocksalt (Fm3m, No. 225) phase. The choice of the LDA functional is consistent with the previous work [18]. Electronic structure and transport properties were calculated using the HSE06 hybrid functional, with a plane-wave energy cutoff of 520 eV and an  $11 \times 11 \times 11$  Monkhorst-Pack  $k$ -point grid. Structural relaxations were performed via the conjugate-gradient method until all residual Hellmann-Feynman forces and energy were below  $10^{-6}$  eV/Å and  $10^{-8}$  eV.

Phonon calculations utilized a  $5 \times 5 \times 5$  supercell with a  $3 \times 3 \times 3$   $k$ -point mesh in the finite displacement approach. The interatomic interaction cutoff radii for calculating the interatomic force constants (IFCs) were truncated at the fifth- and second-nearest neighbor shells for the third- and fourth-order IFCs, respectively. In the zincblende structure, this protocol results in 188 and 792 independent IFC elements for the third- and fourth-order terms, respectively. For the rocksalt phase, the corresponding numbers were 216 and 872.

### III. RESULTS AND DISCUSSION

#### A. Manifestation of metavalent bonding in rocksalt BeO

The study by Wuttig [19] et al. has revealed that phase-change materials (PCMs) and related compounds exhibit a unique bonding mechanism intermediate between covalent and metallic states, termed “metavalent bonding” in these “incipient metals”. Quantum mechanically, the ground state of such metavalent bonded systems forms a superposition of symmetry-equivalent saturated bond configurations [38], with electrons delocalized across all possible bonding states. This distinctive electronic structure, observed in group IV-VI, V<sub>2</sub>-VI<sub>3</sub>, and V compounds, leads to exceptionally low thermal conductivity, a critical parameter for thermoelectric applications. The long-range nature of these interactions creates a characteristically flat anharmonic potential energy surface, facilitating large atomic fluctuations and enhanced structural entropy that enable rapid phase transitions. These fundamental characteristics explain why metavalent-bonded materials demonstrate outstanding performance in both thermoelectric and phase-change applications.

Materials exhibiting “metavalent bonding” typically display several characteristic features: (i) predominant  $p$ -electron contributions to bonding, (ii) octahedral coordination environments, and (iii) remarkable structure tunability [39–41] due to their exceptional sensitivity to external parameters including temperature, pressure [42] and stoichiometry [43]. These systems further exhibit distinctive dynamical properties such as soft transverse

optical (TO) phonon modes, anomalously large Born effective charges, and high dielectric constants, all of which arise from their unique electronic structure and bonding characteristics.

Recent studies on rs-BeO [18] have revealed that strong electron cloud overlap and Coulomb repulsion cause elongation of the Be–O bond and consequent softening of transverse optical (TO) phonons. Given its deformable rocksalt structure, the VI-group oxygen character, and unexpectedly large static dielectric constant, we hypothesize potential “metavalent bonding” characteristics in rs-BeO. To verify this possibility, we have conducted systematic first-principles calculations.

Following the criteria established by Wuttig [19] et al., we systematically analyze the bonding characteristics as shown in Fig. 1, where materials are classified by plotting electrical conductivity versus Born effective charge with distinct color codes: green for  $p$ -bonded metavalent systems, yellow for  $p$ -bonded covalent compounds, and gray for  $sp^3$  covalent semiconductors. Our calculations place rs-BeO firmly within the metavalent bonding regime (green region), whereas zb-BeO falls into the conventional covalent category (yellow region). Further differentiation by Grüneisen parameter ( $\gamma$ ) reveals that most metavalent materials, including rs-BeO with  $\gamma$  between 2 and 3, exhibit strong anharmonicity that typically correlates with low thermal conductivity, in contrast to modest  $\gamma = 0.94$  of zb-BeO. Band gap analysis (color-coded in Fig. 1) indicates that while most metavalent-bonded systems have gaps below 3 eV (e.g., ZnS at 3.76 eV represents an upper limit in prior studies), both rs-BeO ( $E_g = 10.6$  eV) and zb-BeO ( $E_g = 9.3$  eV) dramatically extend the known range of “incipient metals”. This demonstrates that metavalent bonding can persist even in wide-gap systems.

To elucidate the chemical bonding differences between zb-BeO and rs-BeO, we analyze the distance-dependent second-order IFCs as shown in Fig. 2. Following the methodology proposed by Lee [44] et al., we normalize the IFCs tensor traces to self-interacting terms and compute corresponding 2-norms, both revealing identical trends. Both polymorphs exhibit anomalous non-monotonic IFCs variations that contrast sharply with conventional covalent or ionic systems where interaction strength decays monotonically with distance. Notably, we observe pronounced long-range interactions at specific coordination shells in rs-BeO, particularly the fourth nearest neighbors. The fourth neighbor interactions demonstrate unexpectedly strong coupling despite greater separation distances compared to second and third neighbors that lie outside the metavalent network. This metavalent bonding mechanism further generates unconventional positive IFCs values corresponding to negative spring constants in seventh, ninth and fourteenth neighbor shells, representing a characteristic signature of long-range electronic coupling in metavalent systems. These distinctive second-order IFCs behaviors directly account for the different thermal transport prop-

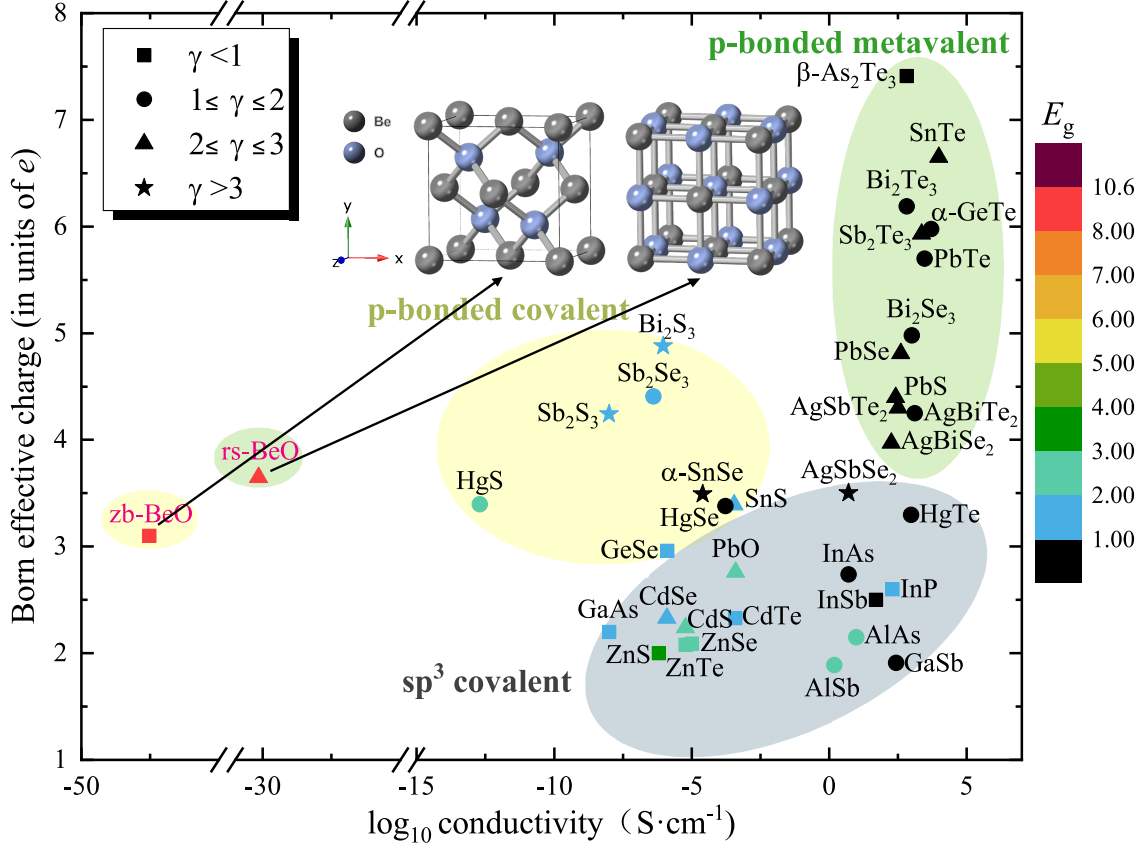


FIG. 1. The conductivity, band gap ( $E_g$ ), Grüneisen parameter ( $\gamma$ ), and Born effective charges of different semiconductors. The band gap can be classified as less than 1 eV, between 1 and 2 eV, between 2 and 3 eV, between 3 and 4 eV, and larger than 8 eV, respectively. Different material dots are represented by black, blue, light green, dark green, and red dots. The  $p$ -bonded metavalent materials,  $p$ -bonded (orthogonal or rocksalt-like) systems, and  $sp^3$  covalent (zincblende-like) crystals are indicated by the green, yellow, and grey ellipses, respectively. Furthermore, black arrows are used to depict the crystal structures of zb-BeO and rs-BeO, with grey and blue spheres representing the Be and O atoms, respectively. All data are available in the Supplementary Material.

erties between the two phases, as will be discussed later.

To evaluate the degree of electron delocalization associated with metavalent bonds, Figs. 2(b) and (e) display the equilibrium charge density distributions. Metavalent bonds typically yield high charge density between atoms, indicating strong interatomic electron sharing [44, 45]. As shown, rs-BeO exhibits more delocalized electronic density between Be atoms than zb-BeO, consistent with stronger bonding interactions. These characteristics align with previously identified signatures of “incipient metals” [46].

Furthermore, Figs. 2(c) and (f) illustrate the charge density response to a small displacement of a central Be atom, considering fourth-nearest-neighbor interactions in the (011) plane. Under identical displacement conditions and cutting planes, rs-BeO demonstrates stronger and more extended charge redistribution compared to zb-BeO. This directly reflects enhanced metavalent bonding, further reinforcing the classification of rs-BeO as a system exhibiting incipient metallic behavior with strong

interatomic electronic coupling.

To further elucidate the differences in electronic bonding between the two phases, Fig. 3 also provides a comprehensive comparison of the electronic band structures and corresponding total and orbital-projected DOS for zb- and rs-BeO. The computed band gaps are 8.7 eV for zb-BeO and 10.5 eV for rs-BeO, which are consistent with previously reported values [18]. From the PDOS, it is seen that the valence bands of both polymorphs are dominated by O-2p states strongly hybridized with Be-2s, forming broad bonding manifolds below the Fermi level. In zb-BeO, the pronounced O- $p$  and Be- $s$  hybridization, correlated with broad valence-band features, indicates strong and localized covalent bonding. Conversely, the conduction-band region of rs-BeO displays comparatively sharper and more localized DOS peaks, originating primarily from Be- $p$  and O- $p$  orbitals. The relatively weak  $s$ - $p$  hybridization in rs-BeO supports a bonding picture that departs from purely directional covalency and aligns more closely with the characteristics of metava-



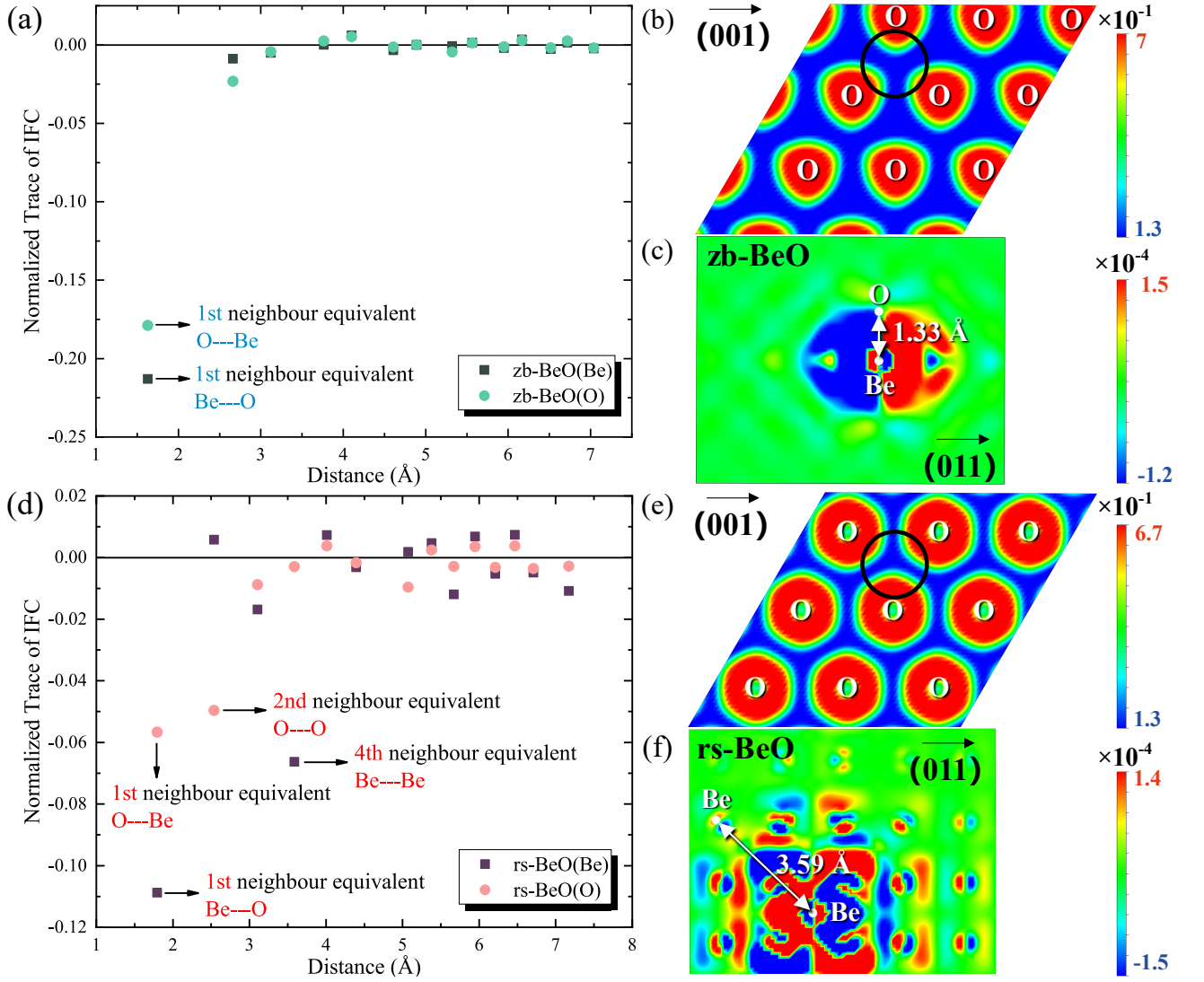


FIG. 2. Normalized traces of interatomic force constants (IFCs) tensors versus atomic distances and charge density disturbance of selected atom pairs and thermal conductivity in (a) zb-BeO and (d) rs-BeO, where different colors denote IFCs with a specific element chosen as the origin atom. The equilibrium electron density distributions of the Be atomic layer in zb-BeO and rs-BeO are shown in (b) and (e), respectively. The color bars show the electron charge density in space. The interatomic area in (b) and (e), where a notable difference in electron departure from the domain is displayed between zb-BeO and rs-BeO is shown by the black circles. Comparison of charge density distortions in zb-BeO and rs-BeO caused by Be atom displacement is shown in (c) and (f). Variations in electron density are shown by color bars in units of  $\text{e}/\text{\AA}^3$ .

lent bonding (i.e., enhanced electron delocalization and reduced bond directionality).

The bonding strength of Be-O pairs in the two phases can also be detected through the projected crystal orbital Hamilton population (pCOHP). By convention, positive values of -pCOHP correspond to bonding contributions, while negative values indicate antibonding character with the Fermi level set at 0 eV [47, 48].

As shown in Fig. 3(c), zb-BeO exhibits strong, well-defined bonding peaks deep in the valence band and a large integrated bond strength, with an integrated -ICOHP of 6.761 eV. This large -ICOHP quantitatively confirms strong Be-O covalency: bonding states are oc-

cupied well below  $E_F$  while anti-bonding states lie largely above it, resulting in a clear bonding, anti-bonding separation and a rigid bonding network. In contrast, it is seen from Fig. 3(f) that rs-BeO displays much smaller -pCOHP amplitudes near the Fermi level and an integrated -ICOHP of only 0.026 eV. The -pCOHP profile of rs-BeO shows a mixture of weak bonding and anti-bonding contributions near  $E_F$ , consistent with the partial occupation of states that are neither strongly bonding nor strongly anti-bonding. This electronic signature further supports the classification of rs-BeO as exhibiting metavalent-like bonding, with greater charge delocalization and reduced directional bond rigidity compared to

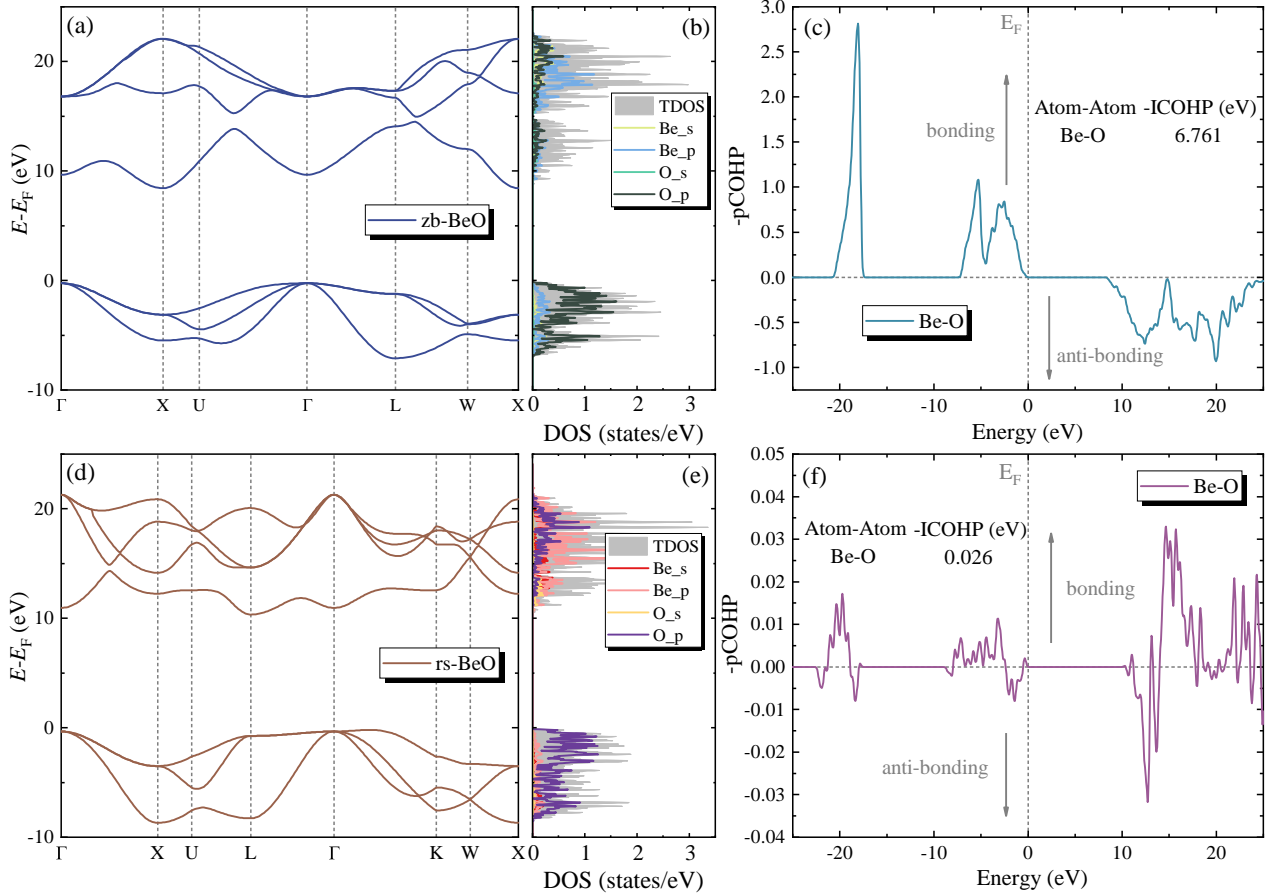


FIG. 3. The electronic properties of zb-BeO and rs-BeO. (a) The electronic band and (b) density of state (DOS) of zb-BeO, where grey shading implies total DOS and yellow, blue, aqua green, and dark green represent the Be-*s*, Be-*p*, O-*s*, and O-*p* orbitals, respectively. (c) and (f) are projected crystal orbital Hamilton population (pCOHP) analysis for the Be-O interactions in zb-BeO and rs-BeO. Negative -pCOHP values correspond to bonding states, whereas positive values denote anti-bonding states. The energy scale is referenced to the Fermi level, which is set at 0 eV. (d-e) are the same with (a-b) where total DOS and the Be-*s*, Be-*p*, O-*s*, and O-*p* orbitals are displayed in red, pink, orange, and violet, respectively.

the zb-BeO phase [18].

### B. Phonon hardening and strong anharmonicity in rocksalt BeO

Building on the bonding analysis, we proceed to examine the anharmonic lattice dynamics of zb-BeO and rs-BeO from 0 to 2000 K using the SCPH theory. As shown in Figs. 4(a) and (b), the phonon spectra of zb-BeO exhibit only minor temperature renormalization, indicating relatively weak anharmonic effects. A clear longitudinal-optical (LO) and transverse-optical (TO) phonon splitting is observed near the  $\Gamma$  point in zb-BeO, originating from its partially ionic Be-O bonds and the macroscopic electric field associated with long-range Coulomb interactions. This LO-TO splitting underscores the polar nature of zb-BeO and its mixed covalent-ionic bonding character, which contribute to higher optical phonon frequencies and enhanced phonon-polarization coupling.

In contrast, the APRN effects in rs-BeO result in overall pronounced phonon hardening with increasing temperature, reflecting the significant role of fourth-order anharmonicity. Notably, the LO-TO splitting is largely suppressed in rs-BeO due to its metavalent bonding nature and stronger electronic screening, which weaken the long-range Coulomb field and diminish polar coupling. These temperature-induced modifications in phonon dispersions directly affect phonon group velocities and scattering phase space, and consequently the  $\kappa_L$ .

The divergence in anharmonic behavior between the two phases actually establishes the correlation between bonding strength and anharmonicity. In zb-BeO, the strong directional Be-O bonds and polar interactions result in weak anharmonicity, as evidenced by the minor renormalization effects observed in its phonon spectrum. In contrast, the more delocalized and less directional metavalent bonding in rs-BeO gives rise to strong anharmonicity, causing a profound renormalization effect on its phonon spectrum.

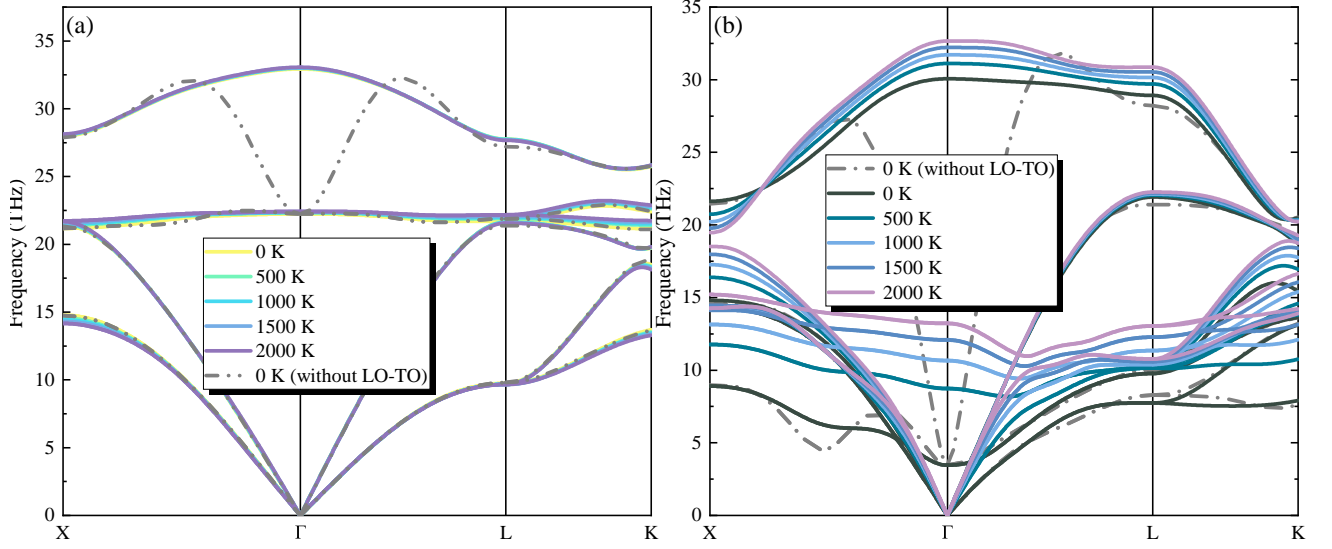


FIG. 4. The phonon dispersions for (a) zb-BeO and (b) rs-BeO with different temperatures, where both are dark grey for the scenario without the LO-TO splitting. In (a), the phonon dispersions at 0 K, 500 K, 1000 K, 1500 K, and 2000 K are shown by the yellow, light green, light blue, dark blue, and purple lines, respectively. In contrast, (b) shows the phonon dispersions at the aforementioned temperatures as dark green, yellow, light blue, dark blue, and pink, respectively.

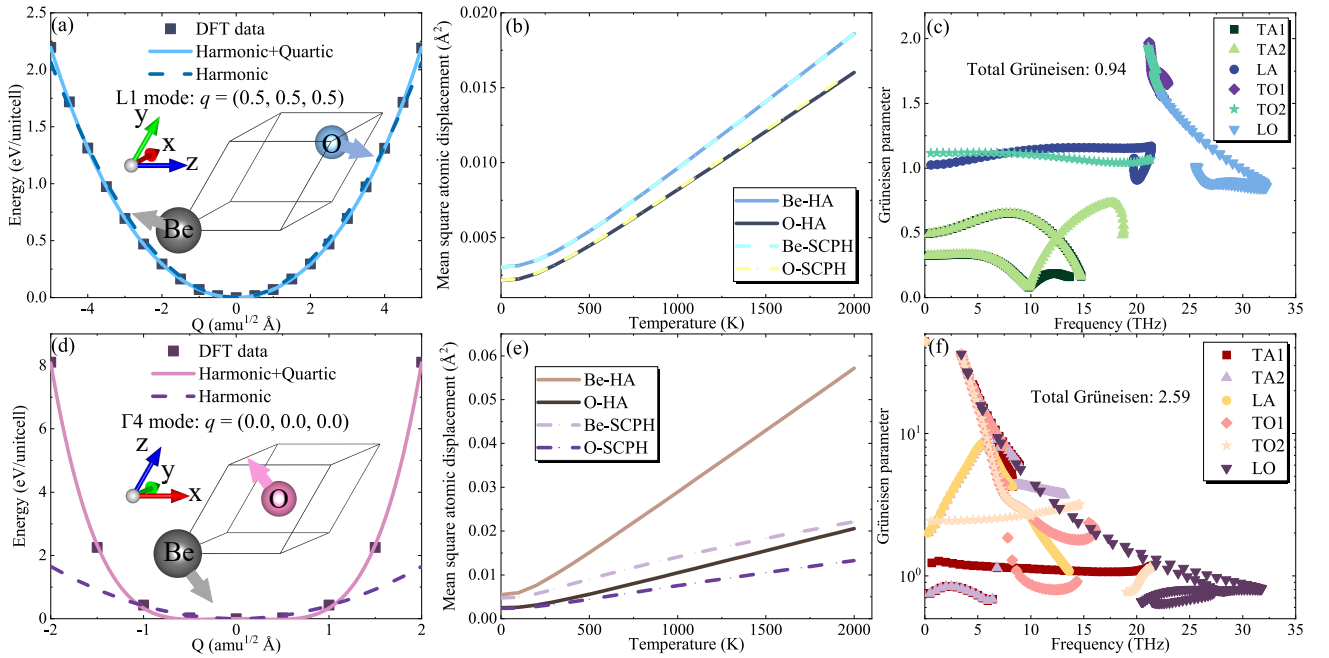


FIG. 5. The potential energy surfaces (PESs), the mean square atomic displacements (MSDs) of Be and O and the Grüneisen parameter for different phonon modes of zb-BeO and rs-BeO. Calculated potential energy surfaces (PESs) of the lowest-lying TA phonon mode are presented for zb-BeO at the  $L$  point and rs-BeO at the  $\Gamma$  point in (a) and (c), respectively. The insets depict the corresponding atomic vibration patterns. The MSDs of Be and O for zb-BeO and rs-BeO are shown in (b) and (e), respectively. In both (b) and (e), the MSDs from the harmonic approximation (HA) and self-consistent phonon (SCPH) method are shown as solid and dashed lines, respectively, for Be and O atoms. Specifically, the HA results use light/dark blue in (b) and flesh/coffee in (e), while the SCPH results use bright blue/bright yellow in (b) and light/deep purple in (e). The Grüneisen parameter is shown in (c) and (f) for the transversal acoustic (TA), longitudinal acoustic (LA), transversal optical (TO), and longitudinal optical (LO) phonon modes at 300 K, respectively. The overall Grüneisen parameter for rs-BeO is 2.59, while that of zb-BeO is 0.94.

The Lyddane–Sachs–Teller (LST) relation connects the longitudinal optical (LO) and transverse optical (TO) phonon frequencies at the  $\Gamma$  point with the static and high-frequency dielectric constants of a polar crystal, and is expressed as [49],

$$\frac{\varepsilon_0}{\varepsilon_\infty} = \left( \frac{\omega_{\text{LO}}}{\omega_{\text{TO}}} \right)^2$$

where  $\varepsilon_0$  and  $\varepsilon_\infty$  are the static and high-frequency dielectric constants, and  $\omega_{\text{LO}}$  and  $\omega_{\text{TO}}$  are the LO and TO phonon frequencies. For zb-BeO,  $\omega_{\text{LO}} = 33.017$  THz,  $\omega_{\text{TO}} = 22.248$  THz,  $\varepsilon_0 = 6.7995$ , and  $\varepsilon_\infty = 3.1016$ , well satisfying the LST relation. In contrast, rs-BeO exhibits  $\omega_{\text{LO}} = 30.063$  THz,  $\omega_{\text{TO}} = 3.459$  THz,  $\varepsilon_0 = 6.7995$ , and  $\varepsilon_\infty = 3.1016$ , clearly violating it. Similarly, the metavalent-bonded material PbTe shows  $\omega_{\text{LO}} = 112.62$   $\text{cm}^{-1}$ ,  $\omega_{\text{TO}} = 48.22$   $\text{cm}^{-1}$  [50],  $\varepsilon_0 = 412 \pm 40$ , and  $\varepsilon_\infty = 31.81 \pm 0.34$  [51], also failing the LST relation. These results suggest that pronounced LST violations may be a characteristic feature of “incipient metals” or metavalently bonded materials.

To understand the physics behind the anharmonicity-induced phonon hardening, we further calculate the potential energy surfaces (PESs) of the lowest-lying TA phonon mode in zb-BeO at the  $\mathbf{L}$  point and the lowest-lying optical mode in rs-BeO at the  $\mathbf{\Gamma}$  point. As shown in Figs. 5(a) and (d), the PESs of these representative phonon modes reveal distinct characteristics between zb-BeO and rs-BeO. In zb-BeO, the L1 acoustic mode at the Brillouin zone boundary exhibits an almost harmonic PES with only minor quartic corrections, consistent with the weak temperature dependence of the phonon dispersions in Fig. 4(a). In contrast, the  $\Gamma_4$  optical mode of rs-BeO displays a markedly U-shaped potential with a significant quartic contribution, which is well captured by a harmonic and quartic fit. This pronounced deviation from harmonic behavior directly accounts for the strong phonon hardening and large temperature-induced frequency shifts observed in Fig. 4(b), confirming significant fourth-order anharmonicity in the rocksalt phase.

The temperature evolution of the atomic mean square atomic displacements (MSDs) further corroborates this finding, as illustrated in Figs. 5(b) and (e). In zb-BeO, the calculated MSDs of both Be and O atoms show only minor differences between the HA and SCPH results, indicating weak anharmonic effects. In stark contrast, the HA-predicted MSDs in rs-BeO deviate significantly from the SCPH results at elevated temperatures, particularly for Be atoms. Notably, the displacement amplitudes of Be atoms in rs-BeO are approximately three times higher than those in zb-BeO, highlighting the much stronger anharmonicity in the former. This behavior implies that the strong quartic anharmonicity in rs-BeO effectively hardens the atomic vibrations and suppresses the phonon population, thereby reducing the MSDs.

The difference in anharmonicity between two phases can be further revealed by the branch-resolved Grüneisen

parameters ( $\gamma$ ) presented in Fig. 5(c) and (f). The total  $\gamma$  values are 0.94 for zb-BeO and 2.59 for rs-BeO, respectively. Notably, the  $\gamma$  of rs-BeO ranks among the highest reported for incipient metals, exceeding those of SnTe (2.1) [52],  $\text{Sb}_2\text{Te}_3$  (2.3) [53], PbSe (2.23) [19], PbS (2.52) [19],  $\text{AgSbTe}_2$  (2.05) [54], and approaching that of  $\text{AgBiSe}_2$  (2.9) [55]. In zb-BeO, the main contributions around  $\sim 20$  THz stem from TO modes with relatively small  $\gamma$ , in line with its stable optical branches and weak anharmonicity in Fig. 4(a). In contrast, rs-BeO exhibits substantially larger  $\gamma$  values for both low-frequency ( $< 10$  THz) acoustic and optical branches, consistent with the strong renormalized phonon dispersion evident in Fig. 4(b). These results demonstrate that the strong anharmonicity in rs-BeO arises primarily from its soft, low-frequency phonon modes, which are highly sensitive to temperature and lattice distortions.

### C. Lattice thermal conductivity

With a reliable lattice dynamics model established, we then investigate the lattice thermal conductivity of zb-BeO and rs-BeO using different levels of theory, and the results are shown in Figs. 6(a) and (b). Our methodology involves different combinations of treatments regarding 4ph scattering and anharmonic renormalization. In zb-BeO, phonon renormalization exhibits only a modest influence on thermal transport. At room temperature, including APRN effects reduces the 3ph-limited  $\kappa_L$  from  $\sim 520$  to  $\sim 485$   $\text{W m}^{-1} \text{K}^{-1}$ , a decrease of less than 7%. Further incorporation of 4ph scattering ( $\kappa_{\text{SCPH}}^{3,4\text{ph}}$ ) leads to a 27% reduction in thermal conductivity, yielding a value of  $\sim 353$   $\text{W m}^{-1} \text{K}^{-1}$  that surpasses that of the vast majority of known semiconductor materials. This high  $\kappa_L$  can be largely attributed to the stiff, covalent bonding in zb-BeO, which results in weak anharmonicity—as reflected in the nearly temperature-invariant phonon dispersions and the small  $\gamma$ .

In stark contrast to zb-BeO, phonon renormalization in rs-BeO leads to a substantial enhancement of its lattice thermal conductivity. Within the 3ph picture, the APRN effects increase the room-temperature  $\kappa_L$  from 12 to 61  $\text{W m}^{-1} \text{K}^{-1}$ , accounting for an increase of 408.33%. When 4ph scattering is further included, the APRN effects result in an increase of  $\kappa_L$  at 300 K from 5 to 23  $\text{W m}^{-1} \text{K}^{-1}$ , corresponding to a 360% enhancement. Concurrently, we observe that the APRN effects significantly weaken the temperature dependence of  $\kappa_L$ . In particular, the  $\kappa_L$  calculated with only 3ph scattering ( $\kappa_{\text{SCPH}}^{3\text{ph}}$ ) even exhibits an upward trend at elevated temperatures. Furthermore, 4ph scattering exerts a pronounced suppression effect on  $\kappa_L$  of rs-BeO. Even at room temperature, it reduces  $\kappa_L$  by 58.33% and 62.3% within the HA and SCPH frameworks, respectively. Additionally, the inclusion of coherent transport is found to have a negligible effect on the  $\kappa_L$  of zb-BeO over the entire temperature range and only a minor contribution



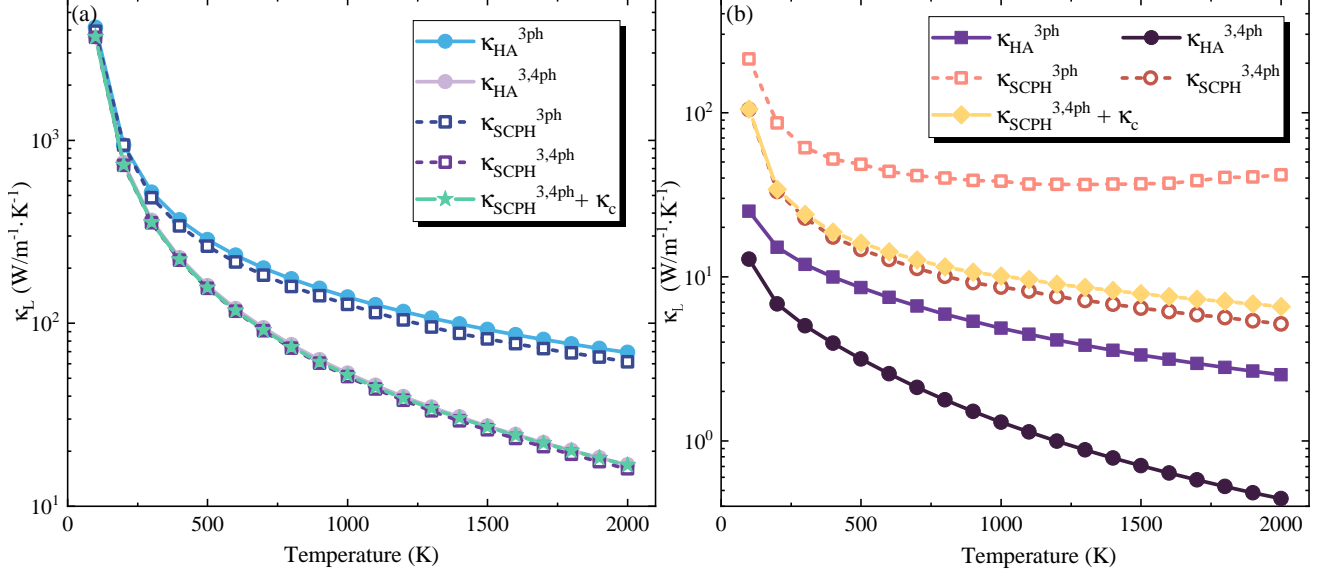


FIG. 6. The lattice thermal conductivity ( $\kappa_L$ ) for zb-BeO and rs-BeO with different temperatures.  $\kappa_L$  Thermal conductivity of (a) zb-BeO and (b) rs-BeO. The harmonic approximation (HA) that takes three-phonon (3ph) interactions into account is represented by “ $\kappa_{HA}^{3ph}$ ”. The harmonic approximation “ $\kappa_{HA}^{3,4ph}$ ” includes both three-phonon (3ph) and four-phonon (4ph) interactions. When examining 3ph interactions, the self-consistent phonon (SCPH) theory is represented by the symbol “ $\kappa_{SCPH}^{3ph}$ ”. For SCPH, 3ph, and 4ph scatterings, “ $\kappa_{SCPH}^{3,4ph}$ ” is used. The coherent phonons is denoted by “ $\kappa_c$ ”. In light green, “ $\kappa_{SCPH}^{3,4ph} + \kappa_c$ ” indicates that “ $\kappa_{SCPH}^{3,4ph}$ ” plus “ $\kappa_c$ ” to determine the total  $\kappa_L$ .

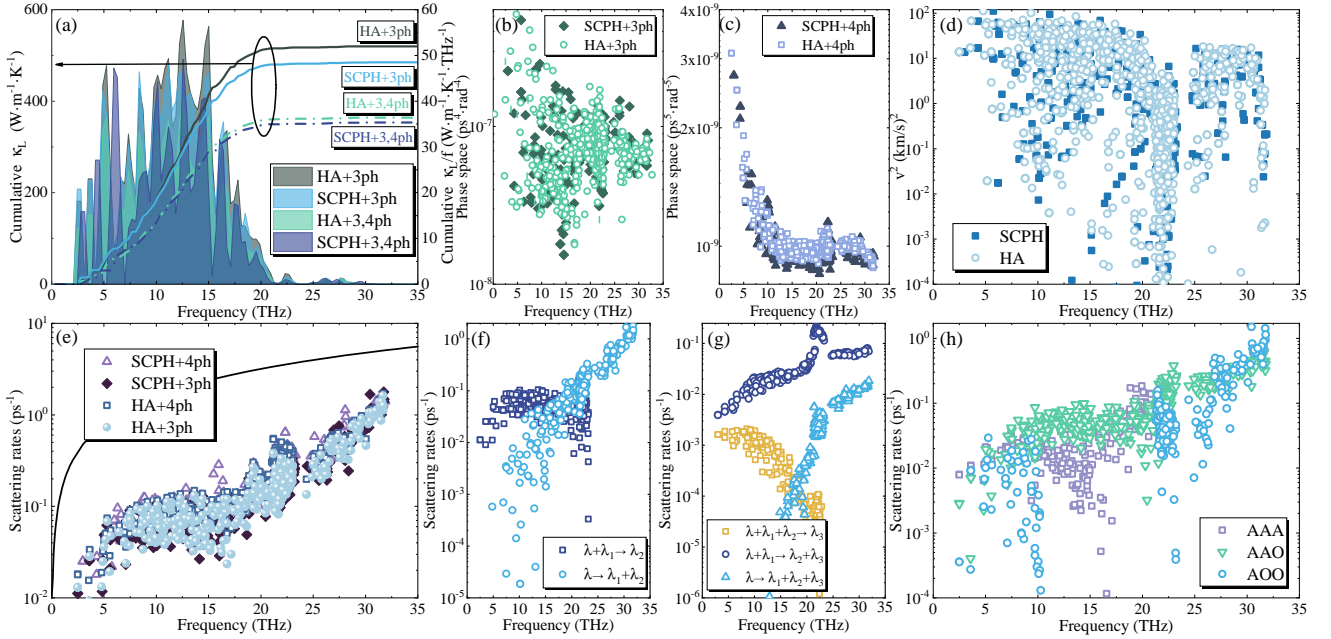


FIG. 7. For the zb-BeO phase at 300 K, (a) the cumulative  $\kappa_L$  and frequency-resolved cumulative  $\kappa_L$  of zb-BeO under various approximation levels [see legend in Fig. 6(a)]. HA+3ph, SCPH+3ph, HA+3,4ph, and SCPH+3,4ph are represented by the dark grey, light blue, green, and dark blue lines, respectively. (b) and (c) phonon scattering phase space. The symbols for HA+3ph, SCPH+3ph, HA+3,4ph, and SCPH+3,4ph are light-green circles, dark-green rhombuses, light-purple triangles, and dark-purple squares, respectively. (d) The square of the phonon group velocity  $v^2$ . (e) Phonon-phonon scattering rates. The Ioffe-Regel limit in time ( $1/\tau = \omega/2\pi$ ) [56] is shown by the solid black line. The deconstructed scattering of 3ph and 4ph into splitting, reconstruction, and combination processes is described in (f) and (g). (h) The AAA, AAO, and AOO scattering channels of 3ph scattering. Acoustic and optical phonons are represented by the letters A and O.

to the  $\kappa_L$  of rs-BeO at high temperatures. Taking all relevant factors into account, the predicted  $\kappa_L$  of rs-BeO reaches  $24 \text{ W m}^{-1} \text{ K}^{-1}$  at room temperature, more than an order of magnitude lower than that of zb-BeO.

The distinct  $\kappa_L$  behaviors of zb-BeO and rs-BeO fundamentally stem from their contrasting bonding and lattice dynamics. The strongly covalent bonds in zb-BeO sustain high phonon group velocities and weak anharmonicity, leading to high  $\kappa_L$  that persists at elevated temperatures. In contrast, the metavalent bonding in rs-BeO, characterized by enhanced charge delocalization and soft phonon modes, induces large anharmonicity, particularly strong quartic anharmonicity, which is responsible for its intrinsically low  $\kappa_L$ . These findings, together with the analysis of anharmonic lattice dynamics, provide a unified understanding of how bonding dictates anharmonicity and ultimately controls heat transport in different BeO phases.

#### D. Microscopic mechanisms of thermal transport

Figs. 7 and 8 systematically illustrate how phonon renormalization influences  $\kappa_L$  and the underlying anharmonic scattering processes in zb-BeO and rs-BeO. At 300 K, the cumulative and frequency-resolved  $\kappa_L$  values obtained from various theoretical approximations. For zb-BeO,  $\kappa_L$  changes negligibly when moving from the harmonic approximation (HA) to the self-consistent phonon (SCPH) framework, confirming that temperature-induced anharmonic renormalization exerts a minimal effect on its heat transport. In sharp contrast, rs-BeO exhibits a pronounced increase in  $\kappa_L$  once renormalization is included. Importantly, this enhancement cannot be attributed to changes in the phonon group velocities, since Fig. 7(d) and Fig. 8(d) show that the squared group velocity ( $v^2$ ) either slightly decreases or remains nearly unchanged after SCPH corrections. Hence, the improved thermal conductivity of rs-BeO originates primarily from the reduction in phonon scattering rates rather than from faster phonon propagation.

To uncover the microscopic origin of this reduction, the available phase space for three-phonon (3ph) and four-phonon (4ph) processes is plotted in Figs. 7(b-c) and Figs. 8(b-c). In zb-BeO, both 3ph and 4ph phase spaces remain nearly constant over the temperature range, reflecting its small intrinsic anharmonicity and the robustness of its covalent framework. By contrast, rs-BeO shows a clear contraction of scattering phase space once anharmonic renormalization is considered. The upward shift of phonon frequencies limits the number of states satisfying the energy-momentum conservation rules, thereby suppressing multi-phonon interactions. This phase-space contraction is the dominant factor that lowers the overall scattering probability and consequently extends phonon lifetimes.

The frequency-resolved total scattering rates are shown in Fig. 7(e) and Fig. 8(e). Without renormalization,

rs-BeO possesses much larger scattering rates than zb-BeO across almost the entire spectrum, especially in the low-frequency region, reflecting its strong lattice anharmonicity. Notably, several modes in rs-BeO exceed the Ioffe-Regel limit ( $1/\tau = \omega/2\pi$ ) [56], indicating that these phonons lose their well-defined quasiparticle nature due to extremely short lifetimes. After incorporating SCPH effects, however, the scattering rates of rs-BeO drop significantly—by nearly an order of magnitude at mid-frequencies—signifying that renormalization restores coherent phonon transport by reducing the number of accessible scattering channels. In contrast, zb-BeO shows almost no variation, confirming that its anharmonic effects are intrinsically weak and temperature-insensitive.

Figs. 7(f-g) and Figs. 8(f-g) further decompose the individual scattering processes. For 3ph events, the merging ( $\lambda + \lambda_1 \rightarrow \lambda_2$ ) and splitting ( $\lambda \rightarrow \lambda_1 + \lambda_2$ ) processes dominate the low- and high-frequency regions, respectively. In rs-BeO, both sub-processes are markedly suppressed upon renormalization because of the reduced phase space and more stringent selection rules. Similarly, for 4ph interactions—including recombination ( $\lambda + \lambda_1 + \lambda_2 \rightarrow \lambda_3$ ), redistribution ( $\lambda + \lambda_1 \rightarrow \lambda_2 + \lambda_3$ ), and splitting ( $\lambda \rightarrow \lambda_1 + \lambda_2 + \lambda_3$ )—the redistribution channel dominates the total 4ph scattering rate, yet all sub-processes weaken notably once SCPH corrections are included. This demonstrates that the phonon lifetime enhancement in rs-BeO stems from the reduced multi-phonon phase space rather than from any modification to the intrinsic interaction strengths.

Finally, Fig. 7(h) and Fig. 8(h) display the mode-resolved 3ph scattering channels, labeled AAA, AAO, AOO, and OOO, corresponding to purely acoustic, mixed acoustic-optical, and purely optical processes, respectively. In zb-BeO, AAO processes dominate and remain largely unchanged upon renormalization, consistent with its stiff covalent bonding and weak coupling between acoustic and optical phonons. In rs-BeO, however, strong AOO and OOO contributions are observed prior to renormalization, reflecting the strong acoustic-optical coupling characteristic of metavalent bonding. These optical-involved channels are substantially suppressed after SCPH corrections, in agreement with the reduction of optical phonon population and the diminished phase space available for optical scattering.

The contrasting thermal transport of zb-BeO and rs-BeO originates from their fundamentally different bonding and lattice dynamics. In zb-BeO, strong directional covalent bonds sustain high phonon velocities, weak anharmonicity, and temperature-insensitive scattering, resulting in exceptionally high and stable  $\kappa_L$ . By contrast, rs-BeO features metavalent bonding with partially delocalized electrons and softer lattice forces, leading to pronounced anharmonicity. Phonon renormalization in rs-BeO moderates these interactions by adjusting phonon frequencies and lifetimes, thereby reducing multi-phonon scattering and stabilizing  $\kappa_L$ . More generally, such renormalization-driven stabilization may oc-

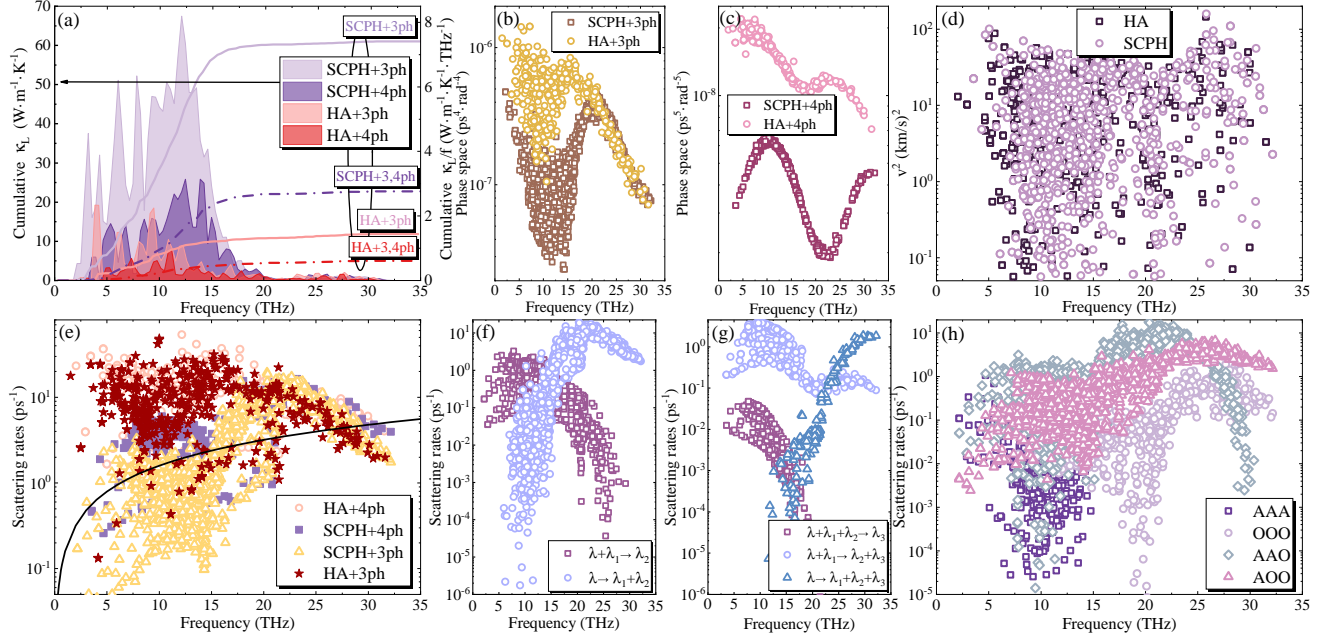


FIG. 8. The microscopic mechanisms of thermal transport of the rs-BeO phase at 300 K [refer to the legend in Fig. 6(b) and Fig. 7].

cur in materials near the covalent–ionic boundary. We propose three indicators for identifying similar “incipient metal” systems: (1) a NaCl-type crystal structure, (2) large Grüneisen parameters ( $>2$ ), and (3) violation of the Lyddane–Sachs–Teller relation. Representative candidates include simple alkali halides such as LiF and LiCl, as well as other light-element compounds with mixed ionic–metavalent bonding, where anharmonic renormalization could likewise moderate strong lattice anharmonicity and stabilize phonon transport.

#### IV. CONCLUSIONS

Our comprehensive investigation of zb-BeO and rs-BeO reveals several fundamental insights into their thermal and electrical transport properties: (i) The  $p$ -bonded metavalent nature of rs-BeO gives rise to enhanced and longer-range inter-atomic interactions. This unique bonding character significantly increases phonon modes hardening, anharmonicity, and expands the available phase space for multi-phonon scattering channels, ultimately resulting in exceptionally low thermal conductivity. (ii) Our detailed analysis demonstrates that several advanced effects must be considered for accurate thermal transport predictions: four-phonon scattering processes, temperature-dependent phonon renormalization, and proper treatment of heat flux operators all contribute substantially and cannot be neglected in these systems. (iii) Electronic conductivity has no relation with “incipient

metal” materials. Strong insulators such as rs-BeO and zb-BeO are good examples. (iv) We identify three key indicators that could guide future searches for “incipient metal” materials: (1) the NaCl-type crystal structure, (2) large Grüneisen parameters exceeding 2, and (3) violation of the Lyddane–Sachs–Teller relation. These characteristics collectively serve as reliable markers for materials exhibiting metavalent bonding behavior for further phonon engineering, promising thermoelectrics and phase-change materials.

#### V. SUPPLEMENTARY MATERIAL

See the supplementary material for the crystal structures and lattice dynamics calculation of zb-BeO and rs-BeO, with the data in Fig. 1 further supported by cited references and normalized traces of interatomic force constants tensors.

#### VI. ACKNOWLEDGMENTS

We acknowledge the support from the National Natural Science Foundation of China (No.52250191 and No.12374038). This work is sponsored by the Key Research and Development Program of the Ministry of Science and Technology (No.2023YFB4604100). We also acknowledge the support by HPC Platform, Xi’an Jiaotong University.

- [1] S. Duman, A. Sütü, S. Bağcı, H. M. Tütüncü, and G. P. Srivastava, “Structural, elastic, electronic, and phonon properties of zinc-blende and wurtzite BeO,” *J. Appl. Phys.* **105**, 033719 (2009).
- [2] A. L. Ivanovskii, I. R. Shein, Yu. N. Makurin, V. S. Kiko, and M. A. Gorbunova, “Electronic structure and properties of beryllium oxide,” *Inorg. Mater.* **45**, 223–234 (2009).
- [3] P. B. Sorokin, A. S. Fedorov, and L. A. Chernozatonskii, “Structure and properties of BeO nanotubes,” *Phys. Solid State* **48**, 398–401 (2006).
- [4] Björn Baumeier, Peter Krüger, and Johannes Pollmann, “Structural, elastic, and electronic properties of SiC, BN, and BeO nanotubes,” *Phys. Rev. B* **76**, 085407 (2007).
- [5] R. M. Hazen and L. W. Finger, “High-pressure and high-temperature crystal chemistry of beryllium oxide,” *J. Appl. Phys.* **59**, 3728–3733 (1986).
- [6] Glen A. Slack and S. B. Austerman, “Thermal conductivity of BeO single crystals,” *J. Appl. Phys.* **42**, 4713–4717 (1971).
- [7] G. Vidal-Valat, J. P. Vidal, K. Kurki-Suonio, and R. Kurki-Suonio, “Multipole analysis of X-ray diffraction data on BeO,” *Acta Crystallogr. A* **43**, 540–550 (1987).
- [8] Zhang Qi-Li, Zhang Ping, Song Hai-Feng, and Liu Hai-Feng, “Mean-field potential calculations of high-pressure equation of state for BeO,” *Chin. Phys. B* **17**, 1341 (2008).
- [9] D.M. Roessler, W.C. Walker, and Eugene Loh, “Electronic spectrum of crystalline beryllium oxide,” *J. Phys. Chem. Solids* **30**, 157–167 (1969).
- [10] Urszula D Wdowik, “Structural stability and thermal properties of BeO from the quasiharmonic approximation,” *J. Phys.: Condens. Matter* **22**, 045404 (2010).
- [11] Munima B. Sahariah and Subhradip Ghosh, “Dynamical stability and phase transition of BeO under pressure,” *J. Appl. Phys.* **107**, 083520 (2010).
- [12] G. G. BENTLE, “Elastic constants of single-crystal BeO at room temperature,” *J. Am. Ceram. Soc.* **49**, 125–128 (1966).
- [13] Carl F. Cline, Harold L. Dunegan, and Glenn W. Henderson, “Elastic constants of hexagonal BeO, ZnS, and CdSe,” *J. Appl. Phys.* **38**, 1944–1948 (1967).
- [14] Jie Wei, Wei Zhou, Song Li, Pei Shen, Shuai Ren, Alice Hu, and Wenzhong Zhou, “Modified embedded atom method potential for modeling the thermodynamic properties of high thermal conductivity beryllium oxide,” *ACS Omega* **4**, 6339–6346 (2019).
- [15] Alexey Bosak, Karin Schmalzl, Michael Krisch, Wouter van Beek, and Vitaly Kolobanov, “Lattice dynamics of beryllium oxide: Inelastic X-ray scattering and ab initio calculations,” *Phys. Rev. B* **77**, 224303 (2008).
- [16] Linu Malakkal, Barbara Szpunar, Ravi Kiran Siripurapu, Juan Carlos Zuniga, and Jerzy A. Szpunar, “Thermal conductivity of wurtzite and zinc blende cubic phases of BeO from ab initio calculations,” *Solid State Sci.* **65**, 79–87 (2017).
- [17] V Milman and M C Warren, “Elasticity of hexagonal BeO,” *J. Phys.: Condens. Matter* **13**, 241 (2001).
- [18] Ruyue Cao, Qiao-Lin Yang, Hui-Xiong Deng, Su-Huai Wei, John Robertson, and Jun-Wei Luo, “Softening of the optical phonon by reduced interatomic bonding strength without depolarization,” *Nature* **634**, 1080–1085 (2024).
- [19] Matthias Wuttig, Volker L. Deringer, Xavier Gonze, Christophe Bichara, and Jean-Yves Raty, “Incipient metals: Functional materials with a unique bonding mechanism,” *Adv. Mater.* **30**, 1803777 (2018).
- [20] Kostiantyn Shportko, Stephan Kremers, Michael Woda, Dominic Lencer, John Robertson, and Matthias Wuttig, “Resonant bonding in crystalline phase-change materials,” *Nat. Mater.* **7**, 653–658 (2008).
- [21] Matthias Wuttig, “Phase change materials: The importance of resonance bonding,” *Phys. Status Solidi B* **246**, 1820–1825 (2009).
- [22] Mohit Raghuwanshi, Oana Cojocaru-Mirédin, and Matthias Wuttig, “Investigating bond rupture in resonantly bonded solids by field evaporation of carbon nanotubes,” *Nano Lett.* **20**, 116–121 (2020).
- [23] Jean-Yves Raty, Mathias Schumacher, Pavlo Golub, Volker L. Deringer, Carlo Gatti, and Matthias Wuttig, “A quantum-mechanical map for bonding and properties in solids,” *Adv. Mater.* **31**, 1806280 (2019).
- [24] Matthias Wuttig, Carl-Friedrich Schön, Jakob Lötfering, Pavlo Golub, Carlo Gatti, and Jean-Yves Raty, “Revisiting the nature of chemical bonding in chalcogenides to explain and design their properties,” *Adv. Mater.* **35**, 2208485 (2023).
- [25] Matthias Wuttig, Carl-Friedrich Schön, Dasol Kim, Pavlo Golub, Carlo Gatti, Jean-Yves Raty, Bart J. Kooi, Ángel Martín Pendás, Raagya Arora, and Umesh Waghmare, “Metavalent or hypervalent bonding: Is there a chance for reconciliation?” *Adv. Sci.* **11**, 2308578 (2024).
- [26] Matteo Cagnoni, Daniel Führen, and Matthias Wuttig, “Thermoelectric performance of IV–VI compounds with octahedral-like coordination: A chemical-bonding perspective,” *Adv. Mater.* **30**, 1801787 (2018).
- [27] Yuan Yu, Matteo Cagnoni, Oana Cojocaru-Mirédin, and Matthias Wuttig, “Chalcogenide thermoelectrics empowered by an unconventional bonding mechanism,” *Adv. Funct. Mater.* **30**, 1904862 (2020).
- [28] Michele Simoncelli, Nicola Marzari, and Francesco Mauri, “Unified theory of thermal transport in crystals and glasses,” *Nat. Phys.* **15**, 809–813 (2019).
- [29] Gaston Kané, Michele Lazzeri, and Francesco Mauri, “Zener tunneling in the electrical transport of quasimetallic carbon nanotubes,” *Phys. Rev. B* **86**, 155433 (2012).
- [30] P. Souvatzis, O. Eriksson, M. I. Katsnelson, and S. P. Rudin, “Entropy driven stabilization of energetically unstable crystal structures explained from first principles theory,” *Phys. Rev. Lett.* **100**, 095901 (2008).
- [31] Ion Errea, Matteo Calandra, and Francesco Mauri, “Anharmonic free energies and phonon dispersions from the stochastic self-consistent harmonic approximation: Application to platinum and palladium hydrides,” *Phys. Rev. B* **89**, 064302 (2014).
- [32] Terumasa Tadano and Shinji Tsuneyuki, “Self-consistent phonon calculations of lattice dynamical properties in cubic SrTiO<sub>3</sub> with first-principles anharmonic force constants,” *Phys. Rev. B* **92**, 054301 (2015).
- [33] Yi Xia, Vinay I. Hegde, Koushik Pal, Xia Hua, Dale Gaines, Shane Patel, Jiangang He, Muratahan Aykol,



- and Chris Wolverton, “High-throughput study of lattice thermal conductivity in binary rocksalt and zinc blende compounds including higher-order anharmonicity,” *Phys. Rev. X* **10**, 041029 (2020).
- [34] G. Kresse and J. Furthmüller, “Efficiency of ab-initio total energy calculations for metals and semiconductors using a plane-wave basis set,” *Comp. Mater. Sci* **6**, 15–50 (1996).
- [35] G. Kresse and J. Furthmüller, “Efficient iterative schemes for ab initio total-energy calculations using a plane-wave basis set,” *Phys. Rev. B* **54**, 11169–11186 (1996).
- [36] P. E. Blöchl, “Projector augmented-wave method,” *Phys. Rev. B* **50**, 17953–17979 (1994).
- [37] G. Kresse and D. Joubert, “From ultrasoft pseudopotentials to the projector augmented-wave method,” *Phys. Rev. B* **59**, 1758–1775 (1999).
- [38] G. Lucovsky and R. M. White, “Effects of resonance bonding on the properties of crystalline and amorphous semiconductors,” *Phys. Rev. B* **8**, 660–667 (1973).
- [39] P. B. Littlewood, “The crystal structure of IV-VI compounds. I. classification and description,” *J. Phys. C: Solid State Phys.* **13**, 4855 (1980).
- [40] Kamran Behnia, “Finding merit in dividing neighbors,” *Science* **351**, 124–124 (2016).
- [41] Morrel H. Cohen, L. M. Falicov, and Stuart Golin, “Crystal chemistry and band structures of the group V semimetals and the IV-VI semiconductors,” *IBM J. Res. Dev.* **8**, 215–227 (1964).
- [42] T. Chattopadhyay, J. Pannetier, and H.G. Von Schnering, “Neutron diffraction study of the structural phase transition in SnS and SnSe,” *J. Phys. Chem. Solids* **47**, 879–885 (1986).
- [43] Dominic Lencer, Martin Salinga, Blazej Grabowski, Tilmann Hickel, Jörg Neugebauer, and Matthias Wuttig, “A map for phase-change materials,” *Nat. Mater.* **7**, 972–977 (2008).
- [44] Sangyeop Lee, Keivan Esfarjani, Tengfei Luo, Jiawei Zhou, Zhiting Tian, and Gang Chen, “Resonant bonding leads to low lattice thermal conductivity,” *Nat. Commun.* **5**, 3525 (2014).
- [45] Yi Zhang, Xuezhong Ke, Paul R. C. Kent, Jihui Yang, and Changfeng Chen, “Anomalous lattice dynamics near the ferroelectric instability in PbTe,” *Phys. Rev. Lett.* **107**, 175503 (2011).
- [46] Sheng-Ying Yue, Tashi Xu, and Bolin Liao, “Ultralow thermal conductivity in a two-dimensional material due to surface-enhanced resonant bonding,” *Mater. Today Phys.* **7**, 89–95 (2018).
- [47] Jingxuan Ding, Tyson Lanigan-Atkins, Mario Calderón-Cueva, Arnab Banerjee, Douglas L. Abernathy, Ayman Said, Alexandra Zevalkink, and Olivier Delaire, “Soft anharmonic phonons and ultralow thermal conductivity in  $\text{Mg}_3(\text{Sb,Bi})_2$  thermoelectrics,” *Sci. Adv.* **7**, eabg1449 (2021).
- [48] Yue Wang, Anping Liu, Xiaolong Yang, and Xiaoyuan Zhou, “Anomalous thermal conductivity anisotropy in bulk hexagonal aln induced by structural phase transition,” *Appl. Phys. Lett.* **126**, 202207 (2025).
- [49] Thibault Sohler, Marco Gibertini, Matteo Calandra, Francesco Mauri, and Nicola Marzari, “Breakdown of optical phonons’ splitting in two-dimensional materials,” *Nano Lett.* **17**, 3758–3763 (2017).
- [50] H. W. Leite Alves, A. R. R. Neto, L. M. R. Scolfaro, T. H. Myers, and P. D. Borges, “Lattice contribution to the high dielectric constant of pbte,” *Phys. Rev. B* **87**, 115204 (2013).
- [51] William Cochran, Roger Arthur Cowley, G. Dolling, and M. M. Elcombe, “The crystal dynamics of lead telluride,” *Proceedings of the Royal Society of London. Series A. Mathematical and Physical Sciences* **293**, 433–451 (1966).
- [52] Rafal Knura, Taras Parashchuk, Akira Yoshiasa, and Krzysztof T. Wojciechowski, “Origins of low lattice thermal conductivity of  $\text{Pb}_{1-x}\text{Sn}_x\text{Te}$  alloys for thermoelectric applications,” *Dalton Trans.* **50**, 4323–4334 (2021).
- [53] X. Chen, H. D. Zhou, A. Kiswandhi, I. Miotkowski, Y. P. Chen, P. A. Sharma, A. L. Lima Sharma, M. A. Hekmaty, D. Smirnov, and Z. Jiang, “Thermal expansion coefficients of  $\text{Bi}_2\text{Se}_3$  and  $\text{Sb}_2\text{Te}_3$  crystals from 10 K to 270 K,” *Appl. Phys. Lett.* **99**, 261912 (2011).
- [54] D. T. Morelli, V. Jovovic, and J. P. Heremans, “Intrinsically minimal thermal conductivity in cubic I–V–VI<sub>2</sub> semiconductors,” *Phys. Rev. Lett.* **101**, 035901 (2008).
- [55] Michele D. Nielsen, Vidvuds Ozolins, and Joseph P. Heremans, “Lone pair electrons minimize lattice thermal conductivity,” *Energy Environ. Sci.* **6**, 570–578 (2013).
- [56] Michele Simoncelli, Nicola Marzari, and Francesco Mauri, “Wigner formulation of thermal transport in solids,” *Phys. Rev. X* **12**, 041011 (2022).